Erosion-driven uplift in the Gamburtsev Subglacial Mountains of East Antarctica

G. J. G. Paxman[a,b,*], A. B. Watts[a], F. Ferraccioli[c], T. A. Jordan[c], R. E. Bell[d], S. S. R. Jamieson[b], C. A. Finn[e]

[a] *Department of Earth Sciences, University of Oxford, South Parks Road, Oxford, OX1 3AN, UK*
[b] *Department of Geography, Durham University, Lower Mountjoy, South Road, Durham, DH1 3LE, UK*
[c] *British Antarctic Survey, High Cross, Madingley Road, Cambridge, CB3 0ET, UK*
[d] *Lamont Doherty Earth Observatory of Columbia University, Palisades, New York 10964, USA*
[e] *US Geological Survey, Denver, Colorado 80225, USA*

Abstract

The relative roles of climate and tectonics in mountain building have been widely debated. Central to this debate is the process of flexural uplift in response to valley incision. Here we quantify this process in the Gamburtsev Subglacial Mountains, a paradoxical tectonic feature in cratonic East Antarctica. Previous studies indicate that rifting and strike-slip tectonics may have provided a key trigger for the initial uplift of the Gamburtsevs, but the contribution of more recent valley incision remains to be quantified. Inverse spectral (free-air admittance and Bouguer coherence) methods indicate that, unusually for continents, the coherence between free-air gravity anomalies and bedrock topography is high (>0.5) and that the elastic thickness of the lithosphere is anomalously low (<15 km), in contrast to previously reported values of up to ~70 km. The isostatic effects of two different styles of erosion are quantified: dendritic fluvial incision overprinted by

*Corresponding author. Fax: +44 1913 341801.
Email address: guy.j.paxman@durham.ac.uk (G. J. G. Paxman)

Alpine-style glacial erosion in the Gamburtsevs and outlet glacier-type selective linear erosion in the Lambert Rift, part of the East Antarctic Rift System. 3D flexural models indicate that valley incision has contributed ca. 500 m of peak uplift in the Gamburtsevs and up to 1.2 km in the Lambert Rift, which is consistent with the present-day elevation of Oligocene–Miocene glaciomarine sediments. Overall, we find that 17–25% of Gamburtsev peak uplift can be explained by erosional unloading. These relatively low values are typical of temperate mountain ranges, suggesting that most of the valley incision in the Gamburtsevs occurred prior to widespread glaciation at 34 Ma. The pre-incision topography of the Gamburtsevs lies at 2–2.5 km above sea-level, confirming that they were a key inception point for the development of the East Antarctic Ice Sheet. Tectonic and/or dynamic processes were therefore responsible for ca. 80% of the elevation of the modern Gamburtsev Subglacial Mountains.

Keywords:
East Antarctica, gravitational admittance, flexure, erosion, landscape evolution, paleotopography

1. Introduction

The Gamburtsev Subglacial Mountains (GSM) are located beneath Dome A of the East Antarctic Ice Sheet (EAIS) (Fig. 1). Although the GSM cannot be directly observed, the subglacial landscape has recently been revealed by Antarctica's Gamburtsev Province (AGAP) radar, aerogravity and aeromagnetic data, collected during the International Polar Year (2008–2009) (Bell et al., 2011). The GSM exhibit 2–3 km of relief and a landscape heavily dissected by fluvial and glacial valleys that resembles the European Alps (Bo et al., 2009; Creyts et al., 2014; Rose et al., 2013). Flanking the Gamburtsevs are a series of north–south trending basins interpreted as comprising the East Antarctic Rift System (EARS) (Ferraccioli et al., 2011). When compared to other mountain ranges, the Alpine-style geomorphology of the GSM (Creyts et al., 2014) is paradoxical, since they are located atop Precambrian cratonic lithosphere (Heeszel et al., 2013). This problem is compounded because no in situ geological samples from the GSM exist; their lithology, age and structure remain unknown.

Unravelling the enigmatic topographic evolution of the GSM is particularly important, because (1) this mountain range is thought to have provided a key nucleation site for the development of the EAIS at the Eocene–Oligocene Boundary (DeConto and Pollard, 2003; Rose et al., 2013) and (2) the processes that build intraplate mountains remain poorly understood, and the Gamburtsevs are the most enigmatic intraplate mountain range on Earth.

Permian rifting and Cretaceous strike-slip faulting have been advanced as tectonic triggers for GSM uplift (Ferraccioli et al., 2011). However, the isostatic response to fluvial/glacial valley incision has been suggested to be responsible for the modern relief and geomorphology of the GSM (Ferraccioli et al., 2011), as has been demonstrated in other mountain ranges (e.g. Champagnac et al., 2007). This isostatic uplift has been quantified using simple 2D flexural models (Ferraccioli et al., 2011), but the 3D distribution of erosion and flexure, as well as the influence of the neighbouring Lambert Rift, have not previously been considered. The aim of this study is to quantify the spatial distribution of Cenozoic fluvial and glacial erosion and the associated isostatic response prior to and during the early stages of EAIS development in order to determine whether this effect was sufficient to drive a substantial part of the uplift of the GSM.

To address this question, the AGAP radar and aerogravity data were used to estimate the effective elastic thickness of the lithosphere (T_e) and the amount and distribution of eroded material in the Gamburtsev region. 3D flexural models were used to calculate the resulting flexural uplift induced by valley incision for different T_e scenarios, and thereby estimate the pre-incision elevation of the GSM. The age of fluvial incision in the GSM was constrained using a landscape evolution model. The main findings are that the processes of valley incision in the GSM predominantly occurred in a temperate climate, and that the Gamburtsevs were at 2–2.5 km elevation prior to the Eocene–Oligocene Boundary.

2. Aerogeophysical Data Acquisition and Reduction

The acquisition of AGAP airborne geophysical data took place between 2$^{\text{nd}}$ December 2008 and 16$^{\text{th}}$ January 2009. Two de Havilland Canada Twin Otter aircraft successfully obtained 120,000 line-km of radio-echo sounding (RES), aeromagnetic and aerogravity data over the GSM and adjacent Lambert Rift. The survey comprised flight lines oriented north–south, with 5 km horizontal spacing. East–west tie lines intersected the main lines every 33 km.

2.1. Surface and Bedrock Topography

Mapping of surface and bedrock topography was carried out using a wing-mounted RES system. RES data were acquired using ice-penetrating radars with a 150 MHz carrier frequency and 15–20 MHz bandwidths, which sample the ice at 2 m intervals along the flight-track (Creyts et al., 2014). Kinematic GPS provided location and altitude data accurate to ~5 cm.

The two-way travel time (TWTT) for the ice surface reflector was multiplied by the radar velocity in air (300 m/μs) to give the terrain clearance of the aircraft.

The difference between the altitude of the aircraft and the terrain clearance is the surface elevation. The difference in TWTT between the bed and ice surface reflectors gives the TWTT in the ice, which is depth converted to an ice thickness using an ice radar velocity of 168 m/μs, with an additional 10 m correction for the firn layer. The difference between the surface elevation and the ice thickness gives the bed elevation. Bed elevations were measured relative to the WGS-84 ellipsoid. The root mean square (RMS) cross-over error was 64 m (Creyts et al., 2014).

The radar data were gridded using a 'nearest neighbour' gridding routine (GMT's *nearneighbor* module (Wessel et al., 2013)) with a grid spacing of 1 km and search radius of 5 km. To form a complete bedrock topography grid for the East Antarctica, data gaps in the grid were filled using the Bedmap2 compilation (Fretwell et al., 2013). This maintained the high resolution of the AGAP data while avoiding excessive computational demand. Grid profiles compare favourably with real RES data (Fig. 2). While gridding causes some of the resolution to be lost, the grid picks out the sharp and high local relief observed in the radar data. Radar-derived bedrock topography data are essential for the spectral analysis carried out in this study, as they guarantee independence of the gravity and topography grids.

2.2. Aerogravity

The UK aircraft acquired aerogravity data using a LaCoste-Romberg S-83 air-sea gravimeter (Jordan et al., 2007). The lines were flown in a stepped pattern with a maximum altitude of 4,600 m over Dome A. The US aircraft used a Sander Geophysics AIRGrav airborne gravity system (Studinger et al., 2008); these lines were flown at a constant terrain clearance not in excess of 500 m. Corrections were applied for the vertical accelerations that act on the aircraft, the Eötvös effect (which depends on speed and heading), and the 'cross-coupling' between the horizontal and vertical accelerations. Data were tied to a base station at McMurdo Station using a LaCoste-Romberg land gravimeter, thereby converting relative gravity to absolute values. Gravity data from the two aircraft were combined and filtered using a 9 km half-wavelength low-pass space-domain kernel filter (Holt et al., 2006). They were then upward continued to a uniform altitude of 4,600 m above the ellipsoid (corresponding to the maximum flight altitude). After reduction, filtering and upward continuation, the overall RMS cross-over error of the free-air gravity anomaly (FAA) data was 2 mGal.

The FAA data were 'nearest neighbour' gridded with a horizontal spacing of 1 km and search radius of 5 km. Long-wavelength Gravity field and steady-state Ocean Circulation Explorer (GOCE) satellite gravity models (Yi et al., 2013) were resampled to 1 km, upward continued to the 4,600 m geodetic datum and used to fill in data gaps surrounding the main AGAP FAA grid. This formed a complete FAA grid for East Antarctica (Fig. 2).

Gravity anomalies arise from undulating interfaces across which there is a density change. In order to calculate a Bouguer correction, the gravity effects of (1) the ice surface and (2) the ice-bed interface were calculated using Parker's expression for the gravity effect of an undulating interface of uniform density contrast (Parker, 1972) (Supplementary Fig. 1). The applied reduction densities for air, ice and rock were 0, 915 and 2670 kgm^{-3}, respectively. The correction for the ice surface was subtracted from the FAA prior to spectral analysis. Subtraction of both corrections from the FAA produced the complete Bouguer anomaly (Fig. 2), which was median filtered to remove wavelengths shorter than 18 km to match the filtered FAA.

3. Methods

3.1. Gravitational Admittance and Coherence

3.1.1. Theory

There are two standard inverse (spectral) methods used to estimate the effective elastic thickness of the lithosphere, T_e, using gravity and topography data: the free-air admittance and the Bouguer coherence. The admittance, $\boldsymbol{Z}(k)$, is the linear transfer function between the gravity anomaly and topography in the frequency domain (e.g. Kirby, 2014).

$$\boldsymbol{Z}(k) = \frac{\langle \Delta \boldsymbol{g}(\boldsymbol{k}) \cdot \boldsymbol{H}^*(\boldsymbol{k}) \rangle}{\langle \boldsymbol{H}(\boldsymbol{k}) \cdot \boldsymbol{H}^*(\boldsymbol{k}) \rangle} \tag{1}$$

$\Delta \boldsymbol{g}(\boldsymbol{k})$ is the Fourier transform of the observed gravity anomaly, $\boldsymbol{H}(\boldsymbol{k})$ is the Fourier transform of the observed topography, $\boldsymbol{k} = (k_x, k_y)$ is the 2D wavenumber and $k = |\boldsymbol{k}|$, * denotes the complex conjugate and $\langle\,\rangle$ indicates annular averaging of the spectral estimates. Another useful spectral parameter is the coherence, $\gamma^2(k)$, which is expressed as (Kirby, 2014)

$$\gamma^2(k) = \frac{|\langle \Delta \boldsymbol{g}(\boldsymbol{k}) \cdot \boldsymbol{H}^*(\boldsymbol{k}) \rangle|^2}{\langle \Delta \boldsymbol{g}(\boldsymbol{k}) \cdot \Delta \boldsymbol{g}^*(\boldsymbol{k}) \rangle \langle \boldsymbol{H}(\boldsymbol{k}) \cdot \boldsymbol{H}^*(\boldsymbol{k}) \rangle} \tag{2}$$

The coherence is essentially the square of the Pearson product-moment correlation coefficient between gravity and topography computed in the frequency domain (Kirby, 2014). A high coherence indicates that a large fraction of the gravity anomaly is caused by the topography. In this study, 0.5 is used as the threshold between high and low coherence. The phase of the admittance, $\phi(k)$, is defined by (Watts, 2001)

$$\mathrm{e}^{-i\,2\,\phi(k)} = \frac{\boldsymbol{Z}(k)}{\boldsymbol{Z}^*(k)} \tag{3}$$

Where the coherence is high, the phase of the admittance should be close to zero.

The bedrock topography, free-air and Bouguer anomaly grids were projected into a customised Lambert conformal conic projection (with central meridian 80.0°E; southern and northern parallels 83.0°S and 77.0°S; and central scale factor 1:1) in order to minimise distortion. The admittance and coherence were calculated using a standard multitaper method (following McKenzie and Fairhead, 1997; McKenzie, 2003; Pérez-Gussinyé et al., 2004). The calculation was carried out for a particular window in the gravity and topography grids. Too small a window will truncate the long wavelengths that characterise high T_es, causing a bias towards low values. Too large a window will incorporate different geological features; the recovered T_e will be ambiguous. The calculation was therefore carried out for four grid windows of increasing size centred on the GSM (Fig. 3).

3.1.2. Elastic Plate Modelling

Within the range of wavelengths over which elastic flexure of the lithosphere is important (100–1000 km) where the 'roll-over' from high to low admittance occurs, the shape of the admittance and coherence functions are dependent on the rigidity of the lithosphere. Assuming that the lithosphere behaves as an elastic plate over geological timescales, the calculated free-air admittance was compared to a model admittance for a flexed elastic plate overlying an inviscid fluid. The model assumes that the plate is subject to surface loading only and that the density of the crust is uniform and equal to that of the load (the topography). The theoretical admittance for this model is given by (Watts, 2001)

$$\mathbf{Z}(k) = 2\,\pi\,G\,(\rho_c - \rho_i)\,\mathrm{e}^{-kd}\,(1 - \Phi_e(k)\,\mathrm{e}^{-kt}) \tag{4}$$

where

$$\Phi_e(k) = \left[\frac{D\,k^4}{(\rho_m - \rho_c)\,g} + 1\right]^{-1} \tag{5}$$

is the flexural response function, and

$$D = \frac{E\,T_e^3}{12\,(1-\nu^2)} \tag{6}$$

is the flexural rigidity. ρ_c, ρ_i (915 $\mathrm{kgm^{-3}}$) and ρ_m (3330 $\mathrm{kgm^{-3}}$) are the densities of the topography/crust, ice and mantle respectively; d is the mean distance between the observation datum (4,600 m above the ellipsoid) and the ice-bedrock interface; t is the mean crustal thickness; G is the universal gravitational constant; g is the acceleration due to gravity; E is Young's modulus (100 GPa); and ν is Poisson's ratio (0.25).

At wavelengths shorter than the isostatic rollover ($k \geq 0.15$ $\mathrm{radkm^{-1}}$), topography is uncompensated and the admittance is given by (Watts, 2001)

$$\boldsymbol{Z}(k) = 2\,\pi\,G\,(\rho_c - \rho_i)\,\mathrm{e}^{-kd} \tag{7}$$

Taking the logarithm of both sides yields

$$\log_{10}\boldsymbol{Z}(k) = -kd\log_{10}\mathrm{e} + \log_{10}(2\,\pi\,G\,(\rho_c - \rho_i)) \tag{8}$$

$\log_{10}\boldsymbol{Z}(k)$ was plotted against k and a straight line was fitted to the interval corresponding to the uncompensated topography ($0.15 \leq k \leq k(\gamma^2 = 0.5)$ $\mathrm{radkm^{-1}}$) by linear regression (Fig. 3). The interval is capped where the coherence, γ^2, falls below 0.5, which indicates topography no longer dominates the gravity signal. The mean ice-bedrock density contrast ($\rho_c - \rho_i$) and depth (d) were determined from the intercept and the gradient, respectively (Eq (8)). The two remaining free parameters in the model are t and T_e. Theoretical admittance curves were calculated for a range of t/T_e combinations. The statistical best-fitting combination for each window is that which minimised the root mean square (RMS) misfit between the observed and theoretical curves (Fig. 4).

Variation in T_e with window size was illustrated by computing the isostatic response function (IRF) (Watts, 2001),

$$\varphi_e(k) = \frac{\boldsymbol{Z}(k)}{2\,\pi\,G\,(\rho_c - \rho_i)\,\mathrm{e}^{-kd}} \tag{9}$$

which normalises the admittance for d and $\rho_c - \rho_i$ for each window (Fig. 4). The theoretical IRF for an elastic plate model is given by (Watts, 2001)

$$\varphi_e(k) = 1 - \Phi_e(k)\,\mathrm{e}^{-kt} \tag{10}$$

$\varphi_e(k)$ was calculated for a range of T_e values and compared to the observed IRF (Fig. 4).

The coherence between the Bouguer anomaly and bedrock topography - the 'Bouguer coherence' - was also modelled for a flexed elastic plate overlying an inviscid fluid. The mean crustal density and thickness for each window derived from the free-air admittance were used for each Bouguer coherence model. Theoretical Bouguer coherence curves were calculated following the approach of Forsyth (1985), which incorporates internal ('buried') loads with a topographic expression and assumes that surface and buried loads are incoherent. For each window, the best-fitting model T_e was that which minimised the RMS misfit between the observed and theoretical Bouguer coherence (Supplementary Fig. 2).

3.2. Spatial Distribution of Eroded Material

If the spatial distribution of erosion is non-uniform, it is possible for peak elevations to increase, because local erosion is less than uplift driven by the flexural isostatic response to regional erosion. The amplitude and wavelength of the flexural response are dependent on T_e.

Quantification of the spatial distribution of eroded material requires the construction of a peak/summit accordance surface. This is a 3D surface representing the restoration of eroded material to the topography without accounting for the associated isostatic response (Champagnac et al., 2007). In order to construct the accordance surface, the GSM topography was first adjusted for the removal of the present-day ice load. The method used to compute this adjustment is described in the paragraph at the end of this section. Maximum values in the rebounded topography grid were isolated using a circular moving window of fixed 15 km radius and designated as peaks (Champagnac et al., 2007) (Fig. 5a). A window radius of 15 km was used to match the approximate wavelength of peaks and valleys in the GSM. It is assumed that these peaks are remnants of a palaeo-surface, and that incision into this surface has not significantly altered the peaks. A preliminary attempt to identify flat-topped surfaces was abandoned, because the GSM are too heavily incised and because the resolution of the topography grid was insufficient to calculate a slope grid and identify flat surfaces.

A surface was smoothly interpolated between the peaks using GMT's (Wessel et al., 2013) continuous curvature tensional spline algorithm (with a tension factor of 0.5) and smoothed with a 100 km Gaussian filter. Subtracting the ice-rebounded topography (Fig. 5a) from the peak accordance surface (Fig. 5b) gives a map of eroded material (Fig. 5c). This method of constructing a peak accordance surface assumes that the erosion of the peaks is negligible compared to the erosion in the valleys; the calculated amount of eroded material is a minimum estimate. Because of the inaccessibility of the GSM, there are no constraints on peak erosion from thermochronology, cosmogenic nuclide exposure dating or identification of flat-topped peaks. Another limitation is the difficulty of fitting a single surface to a landscape so heavily dissected and affected by multiple regimes of erosion.

The flexural response to the removal of the ice sheet and the eroded material was calculated by solving the general flexure equation for the application of a 2D (un)load, $h(x, y)$, to an elastic plate overlying an inviscid fluid.

$$\nabla^2 \left[D(x, y)\, \nabla^2 w(x, y) \right] + (\rho_m - \rho_{infill})\, g\, w(x, y) = (\rho_{load} - \rho_{displace})\, g\, h(x, y) \quad (11)$$

The density of the load (ρ_{load}) was assumed to be 915 kgm^{-3} for ice and 2670 kgm^{-3} for eroded bedrock. A mantle density (ρ_m) of 3330 kgm^{-3} was used, and the material displaced by the (un)loading ($\rho_{displace}$) and infilling the flexure (ρ_{infill}) was assumed to be air, with a density of 0 kgm^{-3}. The same T_e was used to calculate the flexure ($w(x, y)$) due to both the ice unloading and erosional unloading. We computed the flexure for a variety of T_e scenarios based on the results of the spectral modelling in this study and previously reported estimates (Ferraccioli et al., 2011) in order to test the sensitivity of the magnitude and pattern of flexural uplift to the rigidity of the lithosphere.

4. Results

4.1. Effective Elastic Thickness

By fitting a linear regression line to the portion of the admittance curve corresponding to the uncompensated topography (Fig. 3c) and solving Eq (8), an average shallow bedrock density of 2620–2750 kgm^{-3} was recovered across the different grid windows. A decrease in density from 2750 to 2620 kgm^{-3} as the window size increases from 300 km × 600 km to 900 km × 1200 km (Table 1) is consistent with the inclusion within the windows of a greater proportion of the GSM flanks and rift basins, where the presence of lower density sedimentary rocks is expected. The range of densities obtained is consistent with the averaging of metamorphic basement or igneous rocks in the GSM (2700–2800 kgm^{-3}) and lower density sedimentary rocks in the surrounding basins (2400–2600 kgm^{-3}).

The coherence between the FAA and topography is high over a wide range of wavenumbers, particularly for the smaller windows (Fig. 3). This means there is a large wavenumber band over which to confidently fit a regression line and determine topographic density. The error associated with the admittance translates as errors in ρ_c and d of $\pm$100 kgm^{-3} and $\pm$0.2 km, respectively. The observed mean depth from the geodetic datum to the ice-bed interface, d, for each window is within error of the mean depth recovered from spectral analysis of the uncompensated topography.

The best-fitting T_e derived from the free-air admittance remains constant at 0–1 km for each window, which is illustrated by the computed isostatic response functions (Fig. 4). Bouguer coherences indicate a slightly higher T_e of 5–14 km, with a decrease in T_e as the window size is increased (Table 1; Supplementary Fig. 2). These anomalously low T_e estimates are in contrast with previous estimates that reported instead high T_e values of ca. 70 km beneath the range and lower T_e of ca. 30 km beneath the EARS inferred to surround the GSM (Ferraccioli et al., 2011). These discrepancies in T_e estimates are discussed in section 5.1.

4.2. Amount of Erosion and Flexure

The estimated amount of eroded material in the valleys of the GSM is up to 1.2 km (Fig. 5c). In the Lambert Rift, 1.5–2 km of erosion is estimated, which is consistent with independent estimates from ice sheet erosion models (Jamieson et al., 2010). Detrital thermochronology shows evidence for 2–3 km of localised erosion by the Lambert Glacier since the Early Oligocene (Tochilin et al., 2012; Thomson et al., 2013).

The flexure was first computed by solving Eq (11) using an FFT method (Watts, 2001) for a continuous elastic plate with a uniform T_e of 5 km, a value consistent with the results of free-air admittance and Bouguer coherence modelling in this study. The flexural uplift in the central GSM is 500–700 m, and increases to up to 1400 m in the eastern Lambert Rift (Fig. 5d). Although there is short wavelength spatial variability in the uplift, reflecting the low rigidity of the lithosphere, profiles along strike of and perpendicular to the GSM show the flexural uplift is relatively consistent at 500–700 m throughout the range (Fig. 6).

The calculation was also carried out for T_e = 10, 25 and 50 km. This range of values encompasses the results of the spectral modelling in this study and the average for the Gamburtsev region determined by Ferraccioli et al. (2011). At lower T_e values, there is significant short wavelength spatial variability in the distribution of uplift. High T_e values dampen out the shorter wavelength responses, and the uplift is more widely distributed. In the Lambert Rift, T_e = 5 km permits localised uplift of almost 1.5 km. However, higher T_e values significantly reduce the amount of flexure; the uplift is only 700 m at T_e = 50 km. In the GSM, while the pattern of flexure is sensitive to T_e, the magnitude is relatively insensitive; the average uplift only decreases from 560 m (T_e = 5 km) to 460 m (T_e = 50 km) (Fig. 7; Table 2). Subtracting the flexure from the peak accordance surface gives the pre-incision topography. The pre-incision topography is 2–2.5 km in the GSM for each T_e scenario (Fig. 7).

Because East Antarctica was recently interpreted as a mosaic of distinct provinces that came together during orogenic events (Ferraccioli et al., 2011), significant spatial variations in T_e might be expected. An alternative approach to T_e estimation was adopted by Ferraccioli et al. (2011) who used a 3D inversion based on the spatial convolution of surface and buried loads to determine a spatially variable T_e estimate for East Antarctica at 20 km horizontal resolution (Supplementary Fig. 3). The inversion incorporated bedrock topography, constraints on crustal thickness from seismic receiver function data (Hansen et al., 2010), and the extent of a dense lower crustal body proposed to reconcile misfits between observed and modelled Bouguer anomalies. Ferraccioli et al. (2011) calculate a T_e of ca. 70 km beneath the range, and ca. 30 km in the surrounding EARS.

A model incorporating an elastic plate of spatially variable thickness, using a 3D centred finite-difference technique to solve the general flexure equation, was employed to calculate the amount of flexure for this T_e scenario. In the Lambert Rift, the solution is similar to the case of uniform T_e = 25 km. In the GSM, where the average T_e is closer to 70 km, the amount of flexure is 400–500 m (Fig. 7).

5. Discussion

5.1. Effective Elastic Thickness of the Gamburtsev Lithosphere

Gravitational admittance modelling suggests that the Gamburtsev lithosphere is characterised by low T_e values. The best-fitting T_e for the free-air admittance is 0–1 km across all grid windows, and rises only slightly to 5–14 km for the Bouguer coherence. McKenzie et al. (2015) calculated the free-air admittance between Bedmap2 bedrock topography (Fretwell et al., 2013) and GOCE gravity data and determined a best-fitting average T_e for East Antarctica of 21 km. However, T_e estimation based on a spatial convolution approach suggests that the

Gamburtsev lithosphere is characterised by higher T_e values of ca. 70 km (Ferraccioli et al., 2011).

One reason for such a discrepancy may be the role of buried/internal loads. Bouguer coherence modelling indicates that the ratio of buried loading to surface loading in the Gamburtsev region is approximately one (Supplementary Fig. 2). Negatively buoyant loads within or at the base of the lithosphere increase the curvature of the plate. Fitting the observed admittance with models that only incorporate surface loading will therefore cause T_e to be underestimated. In addition, the windowing method may underestimate T_e because if high rigidity terranes exist within the window, but are relatively localised and surrounded by low rigidity lithosphere, the region will give the appearance of being in local, rather than regional, isostatic equilibrium.

However, the low T_e values are borne out across all window sizes, and even when buried loads are incorporated in the models for the Bouguer coherence (Forsyth, 1985), relatively low T_e values (<15 km) are recovered. In addition, seismic receiver function data indicate crustal thicknesses in excess of 48 km and up to 57 km below the GSM (Hansen et al., 2010; Heeszel et al., 2013). Such high crustal thicknesses are consistent with the long wavelength topography of the GSM being dominated by Airy isostasy. At long wavelengths (>500 km), IRFs (Fig. 4) appear to deviate away from elastic plate flexure curves towards finite positive values of 0.3–0.5. A long wavelength correlation between gravity anomalies and topography is unlikely to be associated with plate flexure, but has been attributed to dynamic processes occurring in the Earth's mantle (Panasyuk and Hager, 2000). This may indicate that the long-wavelength elevated East Antarctic plateau is - in part - dynamically supported by the convecting mantle (O'Donnell and Nyblade, 2014). However, further modelling work is needed in order to better understand the thermotectonic history and architecture of the Gamburtsev lithosphere, and how they link to the effective elastic thickness.

The inverse spectral methods, in particular the Bouguer coherence, have been widely used to estimate T_e in the continents, where estimates vary from a few km to over one hundred km. It has been suggested that such methods tend to overestimate T_e due to the effects of erosion, which preferentially removes the short wavelength components of topography (McKenzie and Fairhead, 1997). In the Gamburtsevs, cold-based ice has protected the topography from erosion since shortly after 34 Ma (Creyts et al., 2014; Rose et al., 2013). In addition, the free-air coherences calculated in this study are among the highest ever reported for continental interiors (Fig. 3). Such high coherences are reminiscent of those observed in the oceans (e.g. Watts, 1978), and are the result of negligible erosion rates in the GSM during the last ten million years or more. Subglacial Antarctica offers a previously unrecognised opportunity to evaluate the use of the inverse spectral method for T_e estimation, particularly where non-erosive ice has preserved short wavelength features of topography and high resolution gravity data exist.

5.2. Palaeoclimate and Timing of Valley Incision

The flexural response to valley incision accounts for, on average, 400–600 m (17–25%) of the GSM elevation. Flexure rarely exceeds 25% of the peak elevation in temperate climates (Gilchrist et al., 1994; Montgomery, 1994). This suggests that the processes of valley incision in the GSM occurred in a more temperate climate, and the landscape has remained unmodified since shortly after 34 Ma (Creyts et al., 2014; Rose et al., 2013). Given that flexure accounts for only 17–25% of the elevation of the GSM, there is a need for tectonic trigger(s) and/or dynamic topography to explain the high pre-incision ancestral elevation of the GSM.

Flexure calculations suggest that glacial incision drove 50–80% on the flanks of the Lambert Rift, depending on the assumed T_e. However it is likely that the Lambert Rift contains sediments of Permian age with densities lower than the value of 2670 kgm^{-3} assumed in the flexure calculations, causing the amount of flexure to be overestimated (Ferraccioli et al., 2011). Using a density of 2350 kgm^{-3} for the eroded material reduces the flexural uplift to 40–70% of the total elevation. It is also likely that the difference between the peak accordance surface and the bedrock topography is attributable not solely due to glacial erosion in the Lambert Rift, but also to tectonic subsidence. This means that 40–70% is an upper bound on the contribution of flexure to flank uplift. However, the calculated 1.2 km of uplift in the Lambert Rift is consistent with the present elevation of Oligocene–Miocene Pagodroma Group glaciomarine sediments on the Fisher Massif, now up to 1.2–1.5 km above sea-level (Hambrey and McKelvey, 2000; Hambrey et al., 2007). Older sediments are found at progressively higher elevations, suggesting that uplift was contemporaneous with deposition. This result implies that a significant amount of post-Eocene uplift on the flanks of the Lambert Rift can be attributed to the isostatic response to intense selective linear erosion by a dynamic Lambert Glacier.

The flexure calculations presented in this study lend support to the hypothesis that significant (2–2.5 km) topography existed in the Gamburtsev region prior to 34 Ma and that the mountains were a key inception point for the development of the EAIS at 34 Ma (Rose et al., 2013). Geomorphometric analysis indicates that an inherited fluvial landscape, which was subsequently modified by glacial erosion, exists within the Gamburtsevs (Rose et al., 2013). One might ask for how long did this fluvial landscape exist prior to glaciation? Dating the age of the fluvial landscape of the GSM would also constrain the timing of primary uplift.

The evolution of the fluvial landscape of the GSM was simulated using a numerical model that solves the stream power equation for fluvial advection and diffusion in a temperate climate (Braun and Willett, 2013) and incorporates the ongoing isostatic response to valley incision (Appendix A). The model incorporated low long-term erosion rates as determined from detrital thermochronology (Cox et al., 2010). These erosion rates (0.01–0.02 km/Myr over the last 250 Ma) are very likely to be a minimum estimate, since they are at the lower end of the range of values derived from cosmogenic nuclide dating in Cenozoic mountain ranges (Matmon et al., 2009). It is also difficult to reconcile such low long-term erosion rates with the observation of coal beds of Permian age (Holdgate et al., 2005) and spores and pollen of palm trees of Eocene age (Pross et al., 2012) in East Antarctica, both of which indicate near-tropical climates. By assuming an erosion rate of 0.01 km/Myr, the modelled landscape age is very likely an absolute maximum.

After 50 Myr, the pattern of incision begins to resemble that of the present-day landscape. By 200 Myr, the modelled landscape closely resembles the observed landscape in terms of relief, amount of incision and position of drainage divides and major valleys (Fig. 8). After 200 Myr, the regional elevation is lowered below what is observed today. Assuming that no fluvial incision has occurred since 30 Ma, the maximum age of the preserved fluvial landscape in the GSM is 230 Ma. This result implies that mountain building occurred in interior East Antarctica after the inferred Grenvillian (Ferraccioli et al., 2011) and Pan-African (An et al.,

2015) orogenic events.

Thermochronological and structural observations are consistent with a phase of exhumation and fault activity in East Antarctica during the Permo-Triassic (250 Ma) (Lisker et al., 2003; Phillips and Läufer, 2009), which is attributed to extension north of the GSM and the formation of the East Antarctic Rift System (EARS) (Ferraccioli et al., 2011). Because 250 Ma is at the very upper limit for the age of the fluvial landscape, Permo-Triassic rifting as the sole mechanism for GSM uplift would necessitate anomalously low erosion rates, indicative of an arid climate, since 250 Ma. Low long-term erosion rates prior to Cenozoic glaciation could be attributed to the long-term maintenance of a dry continental climate in interior East Antarctica, which would likely necessitate large basins such as the Wilkes and Aurora lying above sea-level. The presence of surficial rocks that are particularly resistant to erosion (such as Precambrian metamorphic basement) could also be a contributing factor to low long-term erosion rates.

In the Transantarctic Mountains, which form the boundary between East and West Antarctica, the Ross Orogen was eroded to form the Kukri Peneplain, atop which Devonian–Triassic Beacon Supergroup sediments were deposited in an intracratonic/foreland basin (Elliot et al., 2015). It would appear unlikely that an older (pre-Triassic) orogen in the interior of East Antarctica could survive this protracted period of Palaeozoic erosion and Permo-Carboniferous Gondwana glaciation.

Our results indicate that more recent tectonic/dynamic uplift is needed to explain the high relief and heavily incised landscape of the GSM. A phase of Cretaceous exhumation in East Antarctica is attributed to the break-up of East Gondwana at 130–100 Ma (Lisker et al., 2003; Phillips and Läufer, 2009). This phase of denudation may have been related to transtensional reactivation of the Permo-Triassic EARS (Ferraccioli et al., 2011), although recent interpretations of detrital thermochronology data appear to argue against major Cretaceous exhumation in interior East Antarctica (Tochilin et al., 2012; Thomson et al., 2013).

5.3. Erosion, Climate and Isostasy

The total volume of estimated erosion in the GSM and Eastern Lambert Rift combined is 6.2×10^5 km^3. Jamieson et al. (2005) estimated offshore sediment volumes in Prydz Bay using seismic profiles and the boundaries of glacial and fluvial facies located in ODP ocean sediment cores. They estimate the presence of a minimum of 54,000 km^3 of glaciogenic (ca. 34–0 Ma) and 98,000 km^3 of fluviatile (ca. 118–34 Ma) sediments in Prydz Bay (1.5×10^5 km^3 in total); the total volume may be up to 10 times this value (Jamieson et al., 2005; Wilson et al., 2012). These estimates are therefore in agreement to within an order of magnitude. The discrepancy may arise because of the assumption that the peaks in the GSM have not been lowered, the decrease in density between bedrock and sediment, and because many of the valleys in the Gamburtsevs do not flow towards Prydz Bay, but rather towards the basins of the South Pole, the hinterland of the Transantarctic Mountains and the EARS (Fig. 8a). Much sediment was likely routed towards these interior basins. More detailed geophysical study of these basins is required in order to quantify the thickness of sediment present.

The map of eroded material (Fig. 5c) highlights two fundamentally different styles of erosion - dendritic fluvial incision overprinted by Alpine-style valley glaciers in the GSM and major outlet glacier-type incision in the Lambert Rift. In temperate climates, the contribution of denudational isostasy to peak elevations is limited by geomorphic constraints and erosion of the peaks (Gilchrist et al., 1994;

Whipple et al., 1999). However, selective linear glacial erosion is optimal for creating maximum relief in mountain ranges; basal melting is concentrated beneath the thick ice in the troughs, while neighbouring peaks remain preserved beneath non-erosive cold-based ice or air (Stern et al., 2005; Jamieson et al., 2014). In addition, the relatively long wavelength of incision associated with broad glacial outlets such as the Lambert Glacier or the Beardmore or Byrd Glaciers in the Transantarctic Mountains, compared to the shorter wavelength fluvial or Alpine glacial valleys seen in the GSM, permits greater flexural rebound in response to unloading. The wider wavelength of incision explains why the magnitude of flexure induced by selective linear glacial erosion is more sensitive to T_e than that caused by fluvial incision.

Although the peaks of the Gamburtsevs likely experienced erosion prior to glaciation, they have been unmodified for most of the last 34 Ma (Creyts et al., 2014). While the early ice sheets in the GSM flowed down the existing river valleys (Rose et al., 2013), the modern ice sheet flows orthogonal to (and in places up) the valleys (Rignot et al., 2011). Because ice is incapable of flowing fast over such rough terrain due to high coefficients of basal friction, it remains cold-based and non-erosive, preserving steep topographic gradients and maintaining an unmodified subglacial landscape (Jamieson et al., 2014). By contrast, and despite erosion in the GSM being negligible for millions of years, intense selective linear erosion in the Lambert Rift likely continued from the Oligocene to the Neogene beneath a dynamic Lambert Glacier, which still follows the pre-existing tectonically-controlled rift valley, and drove significant isostatic uplift.

6. Conclusions

In this study, we have used a combination of bedrock topography and gravity data to estimate the elastic thickness of the lithosphere and spatial distribution of erosion in the Gamburtsev Subglacial Mountains, in order to make a new estimate of the amount of elevation that is related to erosion processes. In addition, we examined the antiquity of the inherited fluvial landscape of the Gamburtsevs using a landscape evolution model. Based on the results of these methods, we conclude the following:

1. Free-air admittance and Bouguer coherence modelling indicates that T_e in the Gamburtsev region is anomalously low (<15 km), contrasting with the findings of previous studies (Ferraccioli et al., 2011). This result may be indicative of a weaker-than-expected Gamburtsev lithosphere. However, while T_e does influence the pattern of flexural uplift, it does not have a major influence on the magnitude. Free-air coherences are among the highest ever reported for the continents, reflecting negligible erosion rates during the last ten million years or more.
2. The isostatic response to valley incision accounts for 17–25% of total Gamburtsev elevation, which is typical of incision in temperate climates. The pre-incision topography of the GSM was 2–2.5 km. These findings lend strong independent support to the hypothesis that the mountain range existed prior to the Eocene–Oligocene Boundary, and provided a key site for EAIS nucleation. Selective glacial erosion can account for up to 70% of total uplift in the Lambert Rift, reflecting a markedly different erosive regime that continued throughout the Oligocene–Neogene(?).

3. Assuming low long-term erosion rates, landscape evolution models indicate that the maximum age of the inherited fluvial landscape of the GSM is 230 Ma. While it is unlikely that low erosion rates have persisted in East Antarctica since this time, erosion rates may have been inhibited by the exposure of Precambrian basement and the development of an arid climate since Mesozoic(?) times.
4. The interaction between climate and tectonics remains a source of uncertainty in our understanding of intraplate mountain building. In the Transantarctic Mountains, climate - in the form of glacial incision - plays a large role in the uplift of mountain peaks. In the Gamburtsevs, approximately 80% of peak elevation must be attributed to tectonic/dynamic mechanisms, the nature of which remains unclear.

Acknowledgements

Support for GJGP was provided by the Burdett-Coutts Fund, Department of Earth Sciences, University of Oxford and by St. Edmund Hall. We thank Doug Wilson and Egidio Armadillo for their constructive criticism and helpful comments, which greatly improved the final manuscript. The landscape evolution model was modified from a MATLAB script kindly provided by Thorsten Becker. The figures were prepared using the Generic Mapping Tools (GMT) software package (Wessel et al., 2013). The authors would like to acknowledge the Bundensanstalt für Geowissenschaften und Rohstoffe (BGR) for all the support received for the AGAP mission, and in particular Detlef Damaske for his help in planning the airborne geophysical campaign.

Figure and Table Captions

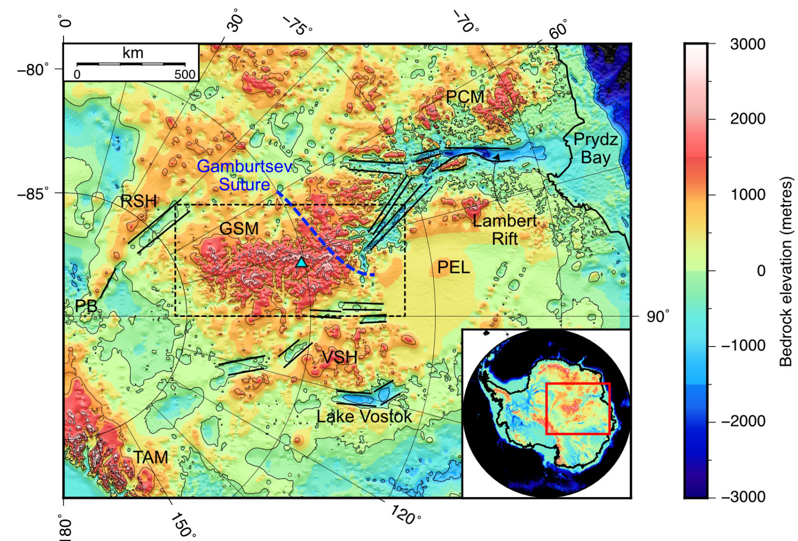

Fig. 1. Geographical and tectonic setting of the Gamburtsev Subglacial Mountains (GSM) within East Antarctica. Bedrock elevation data (above mean sea-level) are from the Bedmap2 compilation (Fretwell et al., 2013). Rift basins (bounded by black lines) comprise the recently defined East Antarctic Rift System (EARS), a proposed trigger for GSM uplift (Ferraccioli et al., 2011). The proposed location of the Gamburtsev Suture (Ferraccioli et al., 2011) is labelled with the blue dashed line. Black dashed box shows the area displayed in Figs 2 and 5. Abbreviations: PB - Polar Basins; PCM - Prince Charles Mountains; PEL - Princess Elizabeth Land; RSH - Recovery Subglacial Highlands; TAM - Transantarctic Mountains; VSH - Vostok Subglacial Highlands. Blue triangle marks Dome A. True scale at 71°S. Inset shows the main study area (red box) within Antarctica. Much of East Antarctica is characterised by an elevated topographic plateau ~1 km above sea-level.

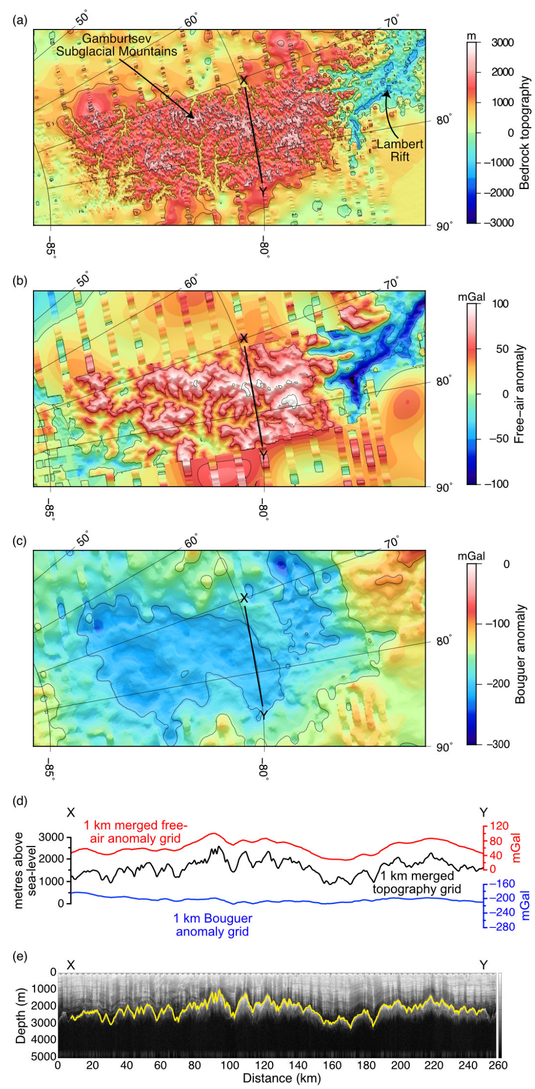

Fig. 2. Bedrock topography and gravity grids for the Gamburtsev region. (a) Bedrock topography. (b) Free-air anomaly. The AGAP free-air gravity data bear a strong resemblance to the bedrock topography, with well-defined, coherent valleys and ridges. (c) Bouguer anomaly. (d) Profile X–Y through the topography and gravity grids, illustrating the strong coherence between the FAA and topography. (e) Radar echogram for the flight line corresponding to profile X–Y. Overlain (yellow) is the bed pick, which was used along with many others to generate the bedrock topography grid.

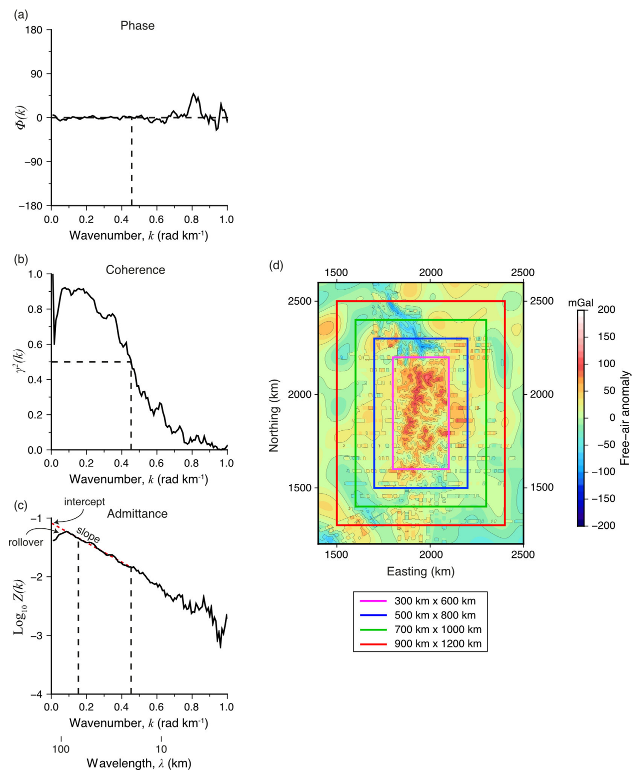

Fig. 3. Spectral parameters for the GSM. (a) Phase, $\phi(k)$. The phase remains close to zero until $k > 0.45$ radkm^{-1}, whereafter high amplitude, short wavelength noise can be seen. (b) Coherence, $\gamma^2(k)$. The coherence is relatively high ($\gamma^2 > 0.5$) for wavenumbers less than 0.5 radkm^{-1}. At shorter wavelengths, noise causes the coherence to drop. (c) Logarithm of the admittance, $\log_{10} \mathbf{Z}(k)$. A straight line (red dashed) was fitted (by least squares regression) to the the section of the curve corresponding to uncompensated topography ($0.15 \leq k \leq k(\gamma^2 = 0.5)$ radkm^{-1}). The slope and y-intercept of this line were used to estimate the mean distance between the 4,600 m geodetic datum and the bedrock topography (d) and the mean density of the topography (ρ_c) within each grid window. (d) Calculation windows in the FAA grid projected into a local Lambert conformal conic projection. The admittance was calculated for a series of four windows of increasing size centred on the GSM. The spectral parameters plotted in (a), (b) and (c) correspond to the 300 km $\times$ 600 km window.

Table 1. Results of the free-air admittance and Bouguer coherence modelling for each analysis window. ρ_c and d were determined by linear regression of the free-air admittance data (in the wavenumber interval 'k range'). The values of free-air and Bouguer T_e are those that minimised the RMS misfit between the calculated and modelled free-air admittance and Bouguer coherence, respectively.

Analysis window (km)	k range (radkm^{-1})	ρ (kgm^{-3})	d (km)	Free-air T_e	Bouguer T_e
300×600	0.156–0.452	2750	3.60	1	14
500×800	0.156–0.400	2660	3.51	0	13
700×1000	0.156–0.382	2620	3.44	0	7
900×1200	0.156–0.369	2620	3.78	0	5

Table 2. Results of the erosional unloading calculations for the variety of T_e scenarios tested. The quoted uplift values are averages for the central Gamburtsev (GSM) and Lambert Rift (LR) regions.

T_e scenario	GSM uplift (m)	LR uplift (m)
Uniform 5 km	560	1250
Uniform 10 km	520	1050
Uniform 25 km	500	900
Uniform 50 km	460	700
Spatially variable	420	920

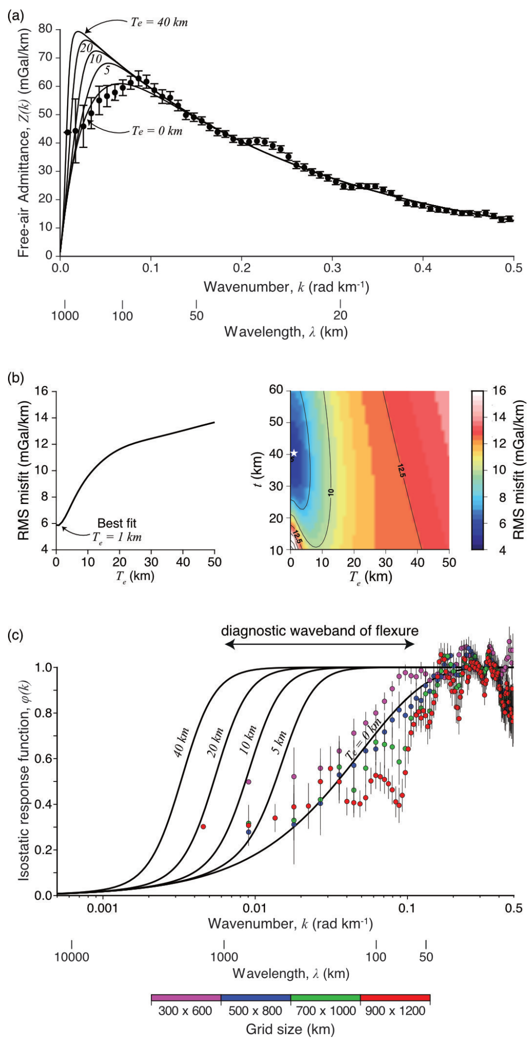

Fig. 4. Free-air admittance modelling results. (a) Free-air gravitational admittance. Black circles with standard error bars represent the calculated admittance $\pm 1\sigma$ for the 300 km $\times$ 600 km window (Fig. 3d). The black lines are model admittance curves for an elastic plate with a crustal thickness of 40 km for varying T_e. (b) RMS misfit between calculated and modelled admittance as a function of t and T_e. Left: the value of T_e that minimises the RMS misfit is 1 km. Right: when RMS misfit is gridded as a function of t and T_e, the best-fitting value of T_e is 1 km, which occurs at t = 41±10 km. (c) Isostatic response functions (IRFs) for all grid windows. Coloured circles with standard error bars represent observed IRFs; solid lines are elastic plate model IRFs. The IRFs are all best-fit by a T_e of 0–5 km. At long wavelengths (> 500 km), the IRFs deviate from the model curves and tend towards finite values of 0.3–0.5. A long wavelength correlation between topography and gravity may indicate a role of mantle dynamics.

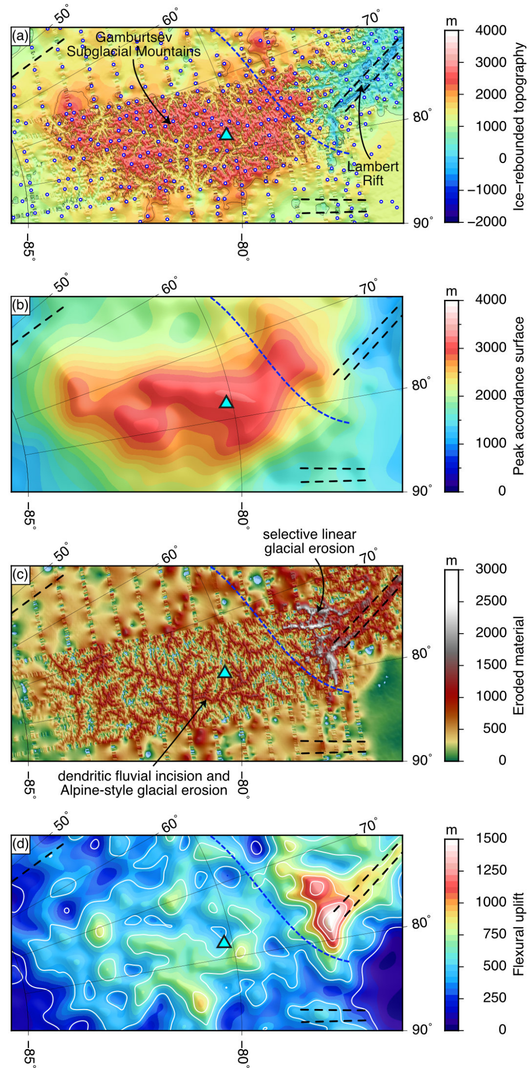

Fig. 5. Erosion-driven uplift in the Gamburtsevs. (a) Subglacial topography adjusted for ice loading assuming a continuous elastic plate model with T_e = 5 km. White circles with blue outlines - peaks identified using a spatial filter. (b) A surface was interpolated between the peaks and filtered with a 100 km Gaussian filter to produce a smoothed peak accordance ('cap') surface. (c) Eroded material. Calculated by subtracting the rebounded topography from the peak accordance surface. Most of the eroded material has been removed from the dendritic network of fluvial/glacial valleys in the GSM and the broad outlet glacial scours of the eastern Lambert Rift. (d) Flexural uplift. A continuous elastic plate model with T_e = 5 km was used. Contour intervals are 200 m. Black dashed lines - rifts of the EARS (Ferraccioli et al., 2011); blue dashed line - Gamburtsev Suture (Ferraccioli et al., 2011); Blue triangle - Dome A.

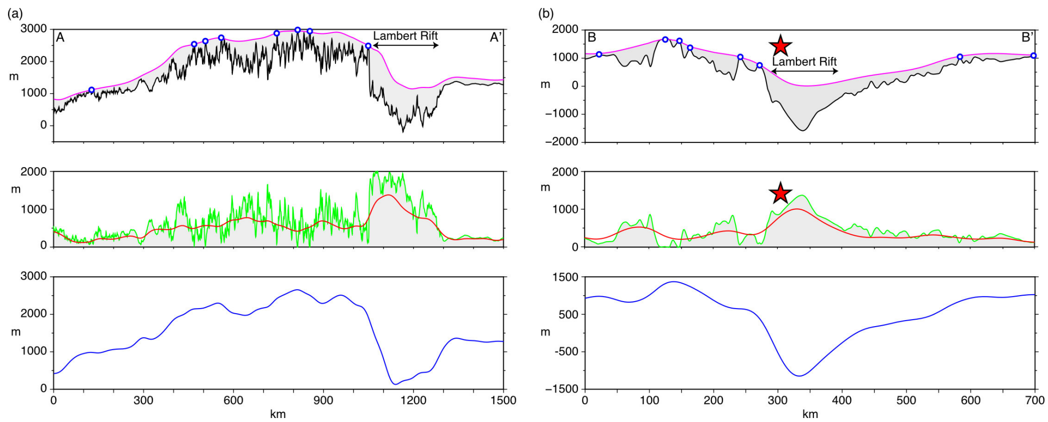

Fig. 6. Profiles (a) through the Gamburtsevs and eastern Lambert Rift from the South Pole basins to Princess Elizabeth Land (A–A') and (b) perpendicular to the strike of Lambert Rift (B–B'). Profile locations are shown in Fig. 7. Upper panel: rebounded (ice-free) topography (black line) and peak accordance surface (purple line). Circles denote peaks used to interpolate the accordance surface. The shaded region represents the eroded material. Middle panel: Eroded material (green line and shaded region) and the isostatic rebound due to the removal of the eroded material for a uniform elastic plate of T_e = 5 km (red line). Flexure throughout the main Gamburtsev mountain range is 500–700 m, but rises to 1.5 km in the Lambert Rift. In (b), the red star represents the present-day elevation of Oligocene–Miocene glaciomarine sediments currently exposed on Fisher Massif that were formed at sea-level. Flexure can account for over 50% of the post-Eocene uplift of these sediments. Lower panel: pre-incision topography (blue line) calculated by subtracting the flexural uplift from the peak accordance surface. This surface represents the ancestral topography that cannot be accounted for by erosion and flexure, and instead reflects primary tectonic/dynamic uplift of the Gamburtsevs and subsidence of the Lambert Rift.

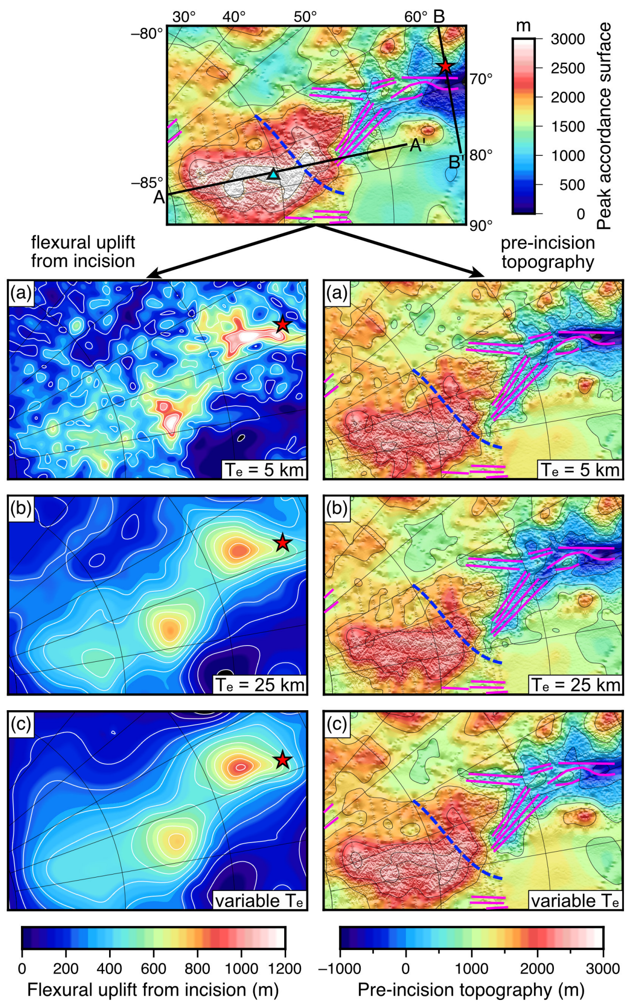

Fig. 7. Sensitivity of flexural uplift to T_e. Upper panel: peak accordance surface (cf. Fig. 5b). Purple lines - EARS; blue dashed line - Gamburtsev Suture; blue triangle - Dome A; red star - Fisher Massif. GSM uplift is partitioned into a flexural and pre-incision component for three T_e scenarios. (a) Continuous elastic plate model with uniform T_e = 5 km (flexural uplift is the same as shown in Fig. 5d). (b) Continuous elastic plate model with uniform T_e = 25 km. (c) Continuous elastic plate model with variable T_e; ca. 70 km beneath the GSM and ca. 30 km in the surrounding EARS. Fisher Massif glaciomarine sediments indicate up to 1.5 km of post-Eocene uplift (Hambrey and McKelvey, 2000). The pre-incision topography of the GSM is 2–2.5 km for every scenario.

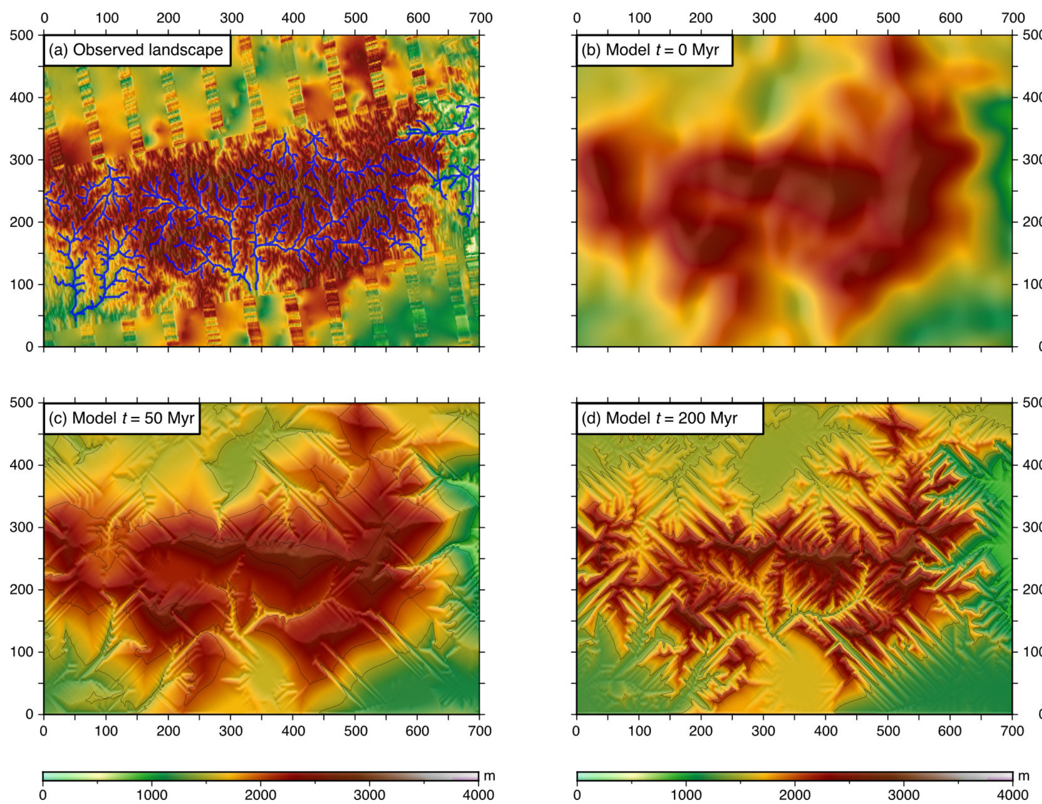

Fig. 8. Modelling the fluvial landscape evolution of the GSM. (a) Present-day Gamburtsev topography corrected for ice loading. Fluvial drainage networks (Rose et al., 2013) are shown in blue. (b) Initial topography for the landscape evolution model (t = 0) is the pre-incision topography calculated for T_e = 5 km. (c) Modelled fluvial landscape after t = 50 Myr. (d) Modelled fluvial landscape after t = 200 Myr.

Appendix A. Landscape Evolution Model

The landscape evolution model solves the combined fluvial incision-hillslope diffusion equation.

$$\frac{\partial h}{\partial t} = U - KA^m \left(\frac{\partial h}{\partial x} \right)^n + \kappa \nabla^2 h \tag{A.1}$$

Physically, this non-linear partial differential equation describes the advection and diffusion of topography, $h(x, y, t)$, by river systems.

- The advection term, $-KA^m \left(\frac{\partial h}{\partial x} \right)^n$, is a power law function of the local drainage area, A, and stream gradient, $\frac{\partial h}{\partial x}$, the quantities that control the rate of bedrock channel erosion (Whipple and Tucker, 1999). K is a dimensional coefficient of erosion, and depends on the erodibility of the bedrock and the amount of rain that falls (which is assumed to be constant throughout the domain). m and n are positive power law exponents, commonly taken as $\frac{1}{3}$ and 1, respectively (Whipple and Tucker, 1999).

- The hillslope diffusion term, $\kappa \nabla^2 h$, takes the form of a typical 2D diffusion equation; the 'erosional diffusivity' is given by κ.

- The uplift term, U, incorporates the ongoing isostatic adjustment to the removal of mass by river systems.

Water is rained onto a regularly spaced topographic surface. Each grid node is surrounded by 8 neighbours. A D8 streamflow algorithm distributes water to the neighbouring grid square with the lowest elevation. Rivers are permitted to flow out of the domain through any of the boundaries. Eq (A.1) is solved numerically at a series of timesteps. A series of assumptions were made in assigning values to the free parameters in Eq (A.1).

The GSM topography is very rugged (Fig. 2), which suggests fluvial advection dominates over diffusion. Preliminary model runs showed that the final landscape is insensitive to κ; the diffusion term was neglected. Eq (A.1) is reduced to

$$\frac{\partial h}{\partial t} = U - KA^{\frac{1}{3}} \frac{\partial h}{\partial x} \tag{A.2}$$

The typical value of the advection constant, K, in modern mountain ranges, such as the European Alps, is $10^{-5}\ m^{\frac{1}{3}} yr^{-1}$ (Whipple and Tucker, 1999). Average Pliocene–Pleistocene erosion rates in the Alps are 0.1–0.5 km/Myr (Champagnac et al., 2007); detrital AFT thermochronology from Prydz Bay sediments suggests minimum long-term erosion rates of 0.01 km/Myr in East Antarctica (Cox et al., 2010). Assuming that the ratio between K and measured erosion rates is the same in the Alps and the Gamburtsevs (which exhibit strikingly similar relief and geomorphology, implying that the erosional regimes were similar), the minimum value of K for the GSM is $2 \times 10^{-7}\ m^{\frac{1}{3}} yr^{-1}$.

The initial topography, $h(x, y, 0)$, was the pre-incision topography grid derived in this study (for $T_e = 5$ km), which represents the cumulative tectonic/dynamic uplift in the absence of incision. The grid was resampled to a resolution of 2 km to ease the computational demand.

The model uses a numerical integration to discretise a continuous process; the upstream drainage area and local slope are calculated at each timestep, as is the uplift due to erosional unloading. The uplift term, $U(x, y, t)$, was calculated using a viscoelastic plate model, which applies the correspondence principle (Brotchie and Silvester, 1969) to derive the viscoelastic flexure ($W(k, t)$) from the initial ($W(k, 0)$) and final ($W(k, \infty)$) elastic response.

$$W(k, t) = W(k, 0)\, \mathrm{e}^{-t/\tau} + [1 - \mathrm{e}^{-t/\tau}]\, [W(k, \infty) - W(k, 0)] \tag{A.3}$$

The viscoelastic parameters assigned to the model were a Maxwell relaxation time, τ of 0.01 Myr (corresponding to an effective viscosity of 10^{22} Pa s), an initial T_e of 90 km (the typical seismic thickness of the lithosphere), and a final T_e of 5 km.

References

An, M., Wiens, D. A., Zhao, Y., Feng, M., Nyblade, A. A., Kanao, M., Li, Y., Maggi, A., Lévêque, J.-J., 2015. S-velocity model and inferred Moho topography beneath the Antarctic Plate from Rayleigh waves. Journal of Geophysical Research: Solid Earth 120 (1), 359–383.

Bell, R. E., Ferraccioli, F., Creyts, T. T., Braaten, D., Corr, H., Das, I., Damaske, D., Frearson, N., Jordan, T., Rose, K., Studinger, M., Wolovick, M., 2011. Widespread persistent thickening of the East Antarctic ice sheet by freezing from the base. Science 331 (6024), 1592–1595.

Bo, S., Siegert, M. J., Mudd, S. M., Sugden, D., Fujita, S., Xiangbin, C., Yunyun, J., Xueyuan, T., Yuansheng, L., 2009. The Gamburtsev mountains and the origin and early evolution of the Antarctic Ice Sheet. Nature 459 (7247), 690–693.

Braun, J., Willett, S. D., 2013. A very efficient O(n), implicit and parallel method to solve the stream power equation governing fluvial incision and landscape evolution. Geomorphology 180-181, 170–179.

Brotchie, J. F., Silvester, R., 1969. On crustal flexure. Journal of Geophysical Research 74 (22), 5240–5252.

Champagnac, J. D., Molnar, P., Anderson, R. S., Sue, C., Delacou, B., 2007. Quaternary erosion-induced isostatic rebound in the western Alps. Geology 35 (3), 195–198.

Cox, S. E., Thomson, S. N., Reiners, P. W., Hemming, S. R., van de Flierdt, T., 2010. Extremely low long-term erosion rates around the Gamburtsev Mountains in interior East Antarctica. Geophysical Research Letters 37 (22), L22307.

Creyts, T. T., Ferraccioli, F., Bell, R. E., Wolovick, M., Corr, H., Rose, K. C., Frearson, N., Damaske, D., Jordan, T., Braaten, D., Finn, C., 2014. Freezing of ridges and water networks preserves the Gamburtsev Subglacial Mountains for millions of years. Geophysical Research Letters 41, 8114–8122.

DeConto, R. M., Pollard, D., 2003. Rapid Cenozoic glaciation of Antarctica induced by declining atmospheric CO2. Nature 421 (6920), 245–249.

Elliot, D. H., Fanning, C. M., Hulett, S. R. W., 2015. Age provinces in the Antarctic craton: Evidence from detrital zircons in Permian strata from the Beardmore Glacier region, Antarctica. Gondwana Research 28 (1), 152–164.

Ferraccioli, F., Finn, C. A., Jordan, T. A., Bell, R. E., Anderson, L. M., Damaske, D., 2011. East Antarctic rifting triggers uplift of the Gamburtsev Mountains. Nature 479 (7373), 388–392.

Forsyth, D. W., 1985. Subsurface loading and estimates of the flexural rigidity of continental lithosphere. Journal of Geophysical Research 90 (B14), 12623–12632.

Fretwell, P., Pritchard, H. D., Vaughan, D. G., Bamber, J. L., Barrand, N. E., Bell, R., Bianchi, C., Bingham, R. G., Blankenship, D. D., Casassa, G., Catania, G., Callens, D., Conway, H., Cook, A. J., Corr, H. F. J., Damaske, D., Damm, V., Ferraccioli, F., Forsberg, R., Fujita, S., Gim, Y., Gogineni, P., Griggs, J. A., Hindmarsh, R. C. A., Holmlund, P., Holt, J. W., Jacobel, R. W., Jenkins, A., Jokat, W., Jordan, T., King, E. C., Kohler, J., Krabill, W., Riger-Kusk, M., Langley, K. A., Leitchenkov, G., Leuschen, C., Luyendyk, B. P., Matsuoka, K., Mouginot, J., Nitsche, F. O., Nogi, Y., Nost, O. A., Popov, S. V., Rignot, E., Rippin, D. M., Rivera, A., Roberts, J., Ross, N., Siegert, M. J., Smith, A. M., Steinhage, D., Studinger, M., Sun, B., Tinto, B. K., Welch, B. C., Wilson, D., Young, D. A., Xiangbin, C., Zirizzotti, A., feb 2013. Bedmap2: improved ice bed, surface and thickness datasets for Antarctica. The Cryosphere 7 (1), 375–393.

Gilchrist, A. R., Summerfield, M. A., Cockburn, H. A. P., 1994. Landscape dissection, isostatic uplift, and the morphologic development of orogens. Geology 22, 963–966.

Hambrey, M. J., Glasser, N., Mckelvey, B., Sugden, D., Fink, D., 2007. Cenozoic landscape evolution of an East Antarctic oasis (Radok Lake area, northern Prince Charles Mountains), and its implications for the glacial and climatic history of Antarctica. Quaternary Science Reviews 26 (5-6), 598–626.

Hambrey, M. J., McKelvey, B., 2000. Major Neogene fluctuations of the East Antarctic ice sheet: Stratigraphic evidence from the Lambert Glacier region. Geology 28 (10), 887–890.

Hansen, S. E., Nyblade, A. A., Heeszel, D. S., Wiens, D. A., Shore, P., Kanao, M., 2010. Crustal structure of the Gamburtsev Mountains, East Antarctica, from S-wave receiver functions and Rayleigh wave phase velocities. Earth and Planetary Science Letters 300 (3-4), 395–401.

Heeszel, D. S., Wiens, D. A., Nyblade, A. A., Hansen, S. E., Kanao, M., An, M., Zhao, Y., 2013. Rayleigh wave constraints on the structure and tectonic history of the Gamburtsev Subglacial Mountains, East Antarctica. Journal of Geophysical Research: Solid Earth 118 (5), 2138–2153.

Holdgate, G. R., McLoughlin, S., Drinnan, A. N., Finkelman, R. B., Willett, J. C., Chiehowsky, L. A., 2005. Inorganic chemistry, petrography and palaeobotany of Permian coals in the Prince Charles Mountains, East Antarctica. International Journal of Coal Geology 63 (1-2 SPEC. ISS.), 156–177.

Holt, J. W., Richter, T. G., Kempf, S. D., Morse, D. L., Blankenship, D. D., 2006. Airborne gravity over Lake Vostok and adjacent highlands of East Antarctica. Geochemistry, Geophysics, Geosystems 7 (11), 1–15.

Jamieson, S. S. R., Hulton, N. R. J., Sugden, D. E., Payne, A. J., Taylor, J., 2005. Cenozoic landscape evolution of the Lambert basin, East Antarctica: the relative role of rivers and ice sheets. Global and Planetary Change 45, 35–49.

Jamieson, S. S. R., Stokes, C. R., Ross, N., Rippin, D. M., Bingham, R. G., Wilson, D. S., Margold, M., Bentley, M. J., 2014. The glacial geomorphology of the Antarctic ice sheet bed. Antarctic Science 26 (06), 724–741.

Jamieson, S. S. R., Sugden, D. E., Hulton, N. R., 2010. The evolution of the subglacial landscape of Antarctica. Earth and Planetary Science Letters 293 (1-2), 1–27.

Jordan, T. A., Ferraccioli, F., Corr, H., Robinson, C., Caneva, G., Armadillo, E., Bozzo, E., Frearson, N., 2007. Linking the Wilkes Subglacial Basin, the Transantarctic Mountains, and the Ross Sea with a New Airborne Gravity Survey. Terra Antarctica Reports 13, 37–54.

Kirby, J. F., 2014. Estimation of the effective elastic thickness of the lithosphere using inverse spectral methods: The state of the art. Tectonophysics 631, 87–116.

Lisker, F., Brown, R., Fabel, D., 2003. Denudational and thermal history along a transect across the Lambert Graben, northern Prince Charles Mountains, Antarctica, derived from apatite fission track thermochronology. Tectonics 22 (5), 1055.

Matmon, A., Simhai, O., Amit, R., Haviv, I., Porat, N., McDonald, E., Benedetti, L., Finkel, R., 2009. Desert pavement-coated surfaces in extreme deserts present the longest-lived landforms on Earth. Bulletin of the Geological Society of America 121 (5-6), 688–697.

McKenzie, D., 2003. Estimating Te in the presence of internal loads. Journal of Geophysical Research 108 (B9), 1–21.

McKenzie, D., Daly, M. C., Priestley, K., 2015. The lithospheric structure of Pangea. Geology 43 (9), 783–786.

McKenzie, D., Fairhead, D., 1997. Estimates of the effective elastic thickness of the continental lithosphere from Bouguer and free air gravity anomalies. Journal of Geophysical Research 102 (B12), 27523–27552.

Montgomery, D. R., 1994. Valley incision and the uplift of mountain peaks. Journal of Geophysical Research 99 (B7), 13913–13921.

O'Donnell, J. P., Nyblade, A. A., 2014. Antarctica's hypsometry and crustal thickness: Implications for the origin of anomalous topography in East Antarctica. Earth and Planetary Science Letters 388, 143–155.

Panasyuk, S. V., Hager, B. H., 2000. Models of isostatic and dynamic topography, geoid anomalies, and their uncertainties. Journal of Geophysical Research 105 (B12), 28199–28209.

Parker, R. L., 1972. The Rapid Calculation of Potential Anomalies. Geophysical Journal of the Royal Astronomical Society 31 (4), 447–455.

Pérez-Gussinyé, M., Lowry, A. R., Watts, A. B., Velicogna, I., 2004. On the recovery of effective elastic thickness using spectral methods: Examples from synthetic data and from the Fennoscandian Shield. Journal of Geophysical Research 109 (B10), 1–20.

Phillips, G., Läufer, A. L., 2009. Brittle deformation relating to the CarboniferousCretaceous evolution of the Lambert Graben, East Antarctica: A precursor for Cenozoic relief development in an intraplate and glaciated region. Tectonophysics 471 (3-4), 216–224.

Pross, J., Contreras, L., Bijl, P. K., Greenwood, D. R., Bohaty, S. M., Schouten, S., Bendle, J. A., Röhl, U., Tauxe, L., Raine, J. I., Huck, C. E., van de Flierdt, T., Jamieson, S. S. R., Stickley, C. E., van de Schootbrugge, B., Escutia, C., Brinkhuis, H., 2012. Persistent near-tropical warmth on the Antarctic continent during the early Eocene epoch. Nature 488 (7409), 73–7.

Rignot, E., Mouginot, J., Scheuchl, B., 2011. Ice Flow of the Antarctic Ice Sheet. Science 333 (6048), 1427–1430.

Rose, K. C., Ferraccioli, F., Jamieson, S. S. R., Bell, R. E., Corr, H., Creyts, T. T., Braaten, D., Jordan, T. A., Fretwell, P. T., Damaske, D., 2013. Early East Antarctic Ice Sheet growth recorded in the landscape of the Gamburtsev Subglacial Mountains. Earth and Planetary Science Letters 375, 1–12.

Stern, T. A., Baxter, A. K., Barrett, P. J., 2005. Isostatic rebound due to glacial erosion within the Transantarctic Mountains. Geology 33 (3), 221–224.

Studinger, M., Bell, R., Frearson, N., 2008. Comparison of AIRGrav and GT-1A airborne gravimeters for research applications. Geophysics 73 (6), 151–161.

Thomson, S. N., Reiners, P. W., Hemming, S. R., Gehrels, G. E., 2013. The contribution of glacial erosion to shaping the hidden landscape of East Antarctica. Nature Geoscience 6 (3), 203–207.

Tochilin, C. J., Reiners, P. W., Thomson, S. N., Gehrels, G. E., Hemming, S. R., Pierce, E. L., 2012. Erosional history of the Prydz Bay sector of East Antarctica from detrital apatite and zircon geo- and thermochronology multidating. Geochemistry, Geophysics, Geosystems 13 (11), 1–21.

Watts, A. B., 1978. An analysis of isostasy in the world's oceans 1. Hawaiian-Emperor Seamount Chain. Journal of Geophysical Research 83 (B12), 5989–6004.

Watts, A. B., 2001. Isostasy and Flexure of the Lithosphere. Cambridge University Press, Cambridge.

Wessel, P., Smith, W. H. F., Scharroo, R., Luis, J., Wobbe, F., 2013. Generic Mapping Tools: Improved Version Released. Eos, Transactions American Geophysical Union 94 (45), 409–410.

Whipple, K. X., Kirby, E., Brocklehurst, S. H., 1999. Geomorphic limits to climate-induced increases in topographic relief. Nature 401, 39–43.

Whipple, K. X., Tucker, G. E., 1999. Dynamics of the stream-power river incision model: Implications for height limits of mountain ranges, landscape response timescales, and research needs. Journal of Geophysical Research 104 (B8), 17661–17674.

Wilson, D. S., Jamieson, S. S. R., Barrett, P. J., Leitchenkov, G., Gohl, K., Larter, R. D., 2012. Antarctic topography at the Eocene-Oligocene boundary. Palaeogeography, Palaeoclimatology, Palaeoecology 335-336, 24–34.

Yi, W., Rummel, R., Gruber, T., apr 2013. Gravity field contribution analysis of GOCE gravitational gradient components. Studia Geophysica et Geodaetica 57 (2), 174–202.